# Utilizing In-Orbit CYGNSS Roll Maneuvers For Improved Level-1 Calibration - Part III: Assessments of Nadir Observables

Mohammad M. Al-Khaldi, *Senior Member, IEEE,* Scott Gleason, *Senior Member, IEEE,* Christopher Ruf, *Life Fellow, IEEE,* Joel T. Johnson, *Fellow, IEEE,* Darren S. McKague, *Member, IEEE,* Anthony Russel, William L. Wells, Tianlin Wang, *Senior Member, IEEE,* Dorina Twigg, Patrick McEnaney and Joshua Synowiec

***Abstract*—Improved characterization of Cyclone Global Navigation Satellite System (CYGNSS) zenith and nadir antenna gain patterns is incorporated into the calibration algorithms for Normalized Bistatic Radar Cross Section (NBRCS) and reflectivity. The updated patterns result from work described in two companion papers (Part I and Part II). Calibration errors directly attributable to antenna gain patterns are reduced by 40-90% across all nadir channels, while NBRCS consistency and uncertainty with respect to reference European Center for Medium-Range Weather Forecasts Reanalysis v5 (ERA5) data are improved by an average of 35%. Similarly, more than 80% of reflectivity measurements exhibit reduced uncertainty and improved correlation with coincident Soil Moisture Active Passive (SMAP) soil moisture measurements. The updated patterns also improve calibration consistency between satellites in the constellation, with a ≈60% reduction in root mean square differences between them.**

***Index Terms*—Cyclone global navigation satellite system, CYGNSS, Global Navigation Satellite Systems Reflectometry (GNSS-R), GPS EIRP, NBRCS, Reflectivity, Level-1 calibration, microwave remote sensing**

## I. Introduction

SENSING of the Earth's dynamic properties using spaceborne L-band observatories is motivated by their reduced sensitivity to the confounding effects of atmospheric constituents as well as heavy rain and cloud cover thereby enabling continuous all weather operation [1], [2]. This enables concurrently achieving sensitivity to a wide range of disparate properties including soil moisture [3]–[6], vegetation indices [7]–[9], ocean wind speed [10], [11], and inland water dynamics [12]–[14] that may be retrieved. Traditionally, sensing these properties has been attempted by radiometers like Soil Moisture and Ocean Salinity (SMOS) [15] or Soil Moisture Active Passive (SMAP) [16], scatterometers like Aquarius [17] or synthetic aperture radars like NASA's NASA-ISRO Synthetic Aperture Radar (NiSAR) [18] or ESA's upcoming Radar Observing System for Europe at L-band (ROSE-L) [19]. The properties of each of these systems makes them well suited for the applications they were intended to support. For example, while systems like SMOS and SMAP exhibit clear sensitivity to soil moisture and related dynamics their coarser spatial resolutions makes their observations ill suited for the mapping of inland water bodies or analyzing inundation, particularly at kilometer level footprints or finer. Conversely, SAR systems' superior spatial resolutions addresses this need. In both cases however, this is achieved at revisit times on the order of 3 days or longer. The costs associated with the design and launch of constellations of these more traditional systems to reduce revisit time are prohibitive, such that insights into dynamic changes occurring on shorter time scales may be limited.

Conversely, constellations of GNSS-R systems like Cyclone Global Navigation Satellite System (CYGNSS) [20] are well suited to address these concurrent needs motivating continued exploration of the means with which the representativeness of their observables to geophysical properties of interest may be enhanced. In this third and final part, the effects the use of updated zenith (direct channel) gain patterns derived using the methodologies explored in Part I (see [21]) and updated nadir gain patterns derived using the methodologies explored in Part II (see [22]) on the mission's Level-1 observables are explored. Compared to preceding characterizations, updated patterns are thought to be more representative of in-orbit behaviors. Observed Normalized Bistatic Radar Cross Section (NBRCS, $\sigma^0$) behaviors are explored in the context of the constellation's ocean surface observations and their correspondence to surface winds while the behavior of measured reflectivities ($\Gamma_{LR}$) over land is explored in the context of their correspondence to soil moisture.

Section II provides a brief background followed by an analysis of NBRCS behaviors in Section III. Practical considerations relating to the use of land reflectivities for the assessment of Level-1 calibration quality are explored in Section IV followed

The research of this article is funded by the NASA Science Mission Directorate through the University of Michigan under Contract NNL13AQ00C.

The research done by Tianlin Wang was carried out at the Jet Propulsion Laboratory, California Institute of Technology, under a contract with the National Aeronautics and Space Administration (80NM0018D0004).

M. M. Al-Khaldi and J. T. Johnson are with the Department of Electrical and Computer Engineering and ElectroScience Laboratory, The Ohio State University, Columbus, OH 43210 USA.

S. Gleason is with Daaxa LLC, Boulder, CO 80307 USA.

C. Ruf and D. S. McKague are with the Department of Climate and Space Sciences and Engineering, University of Michigan, Ann Arbor, MI 48109 USA.

A. Russel is with Muon Space, Mountain View, CA 94043 USA.

W. L. Wells is with Southwest Research Institute, San Antonio, TX 78238 USA.

D. Twigg, P. McEnaney and J. Synowiec are with the Space Physics Research Laboratory, University of Michigan, Ann Arbor, MI 48109 USA.

T. Wang is with NASA Jet Propulsion Laboratory, California Institute of Technology, Pasadena, CA, USA.

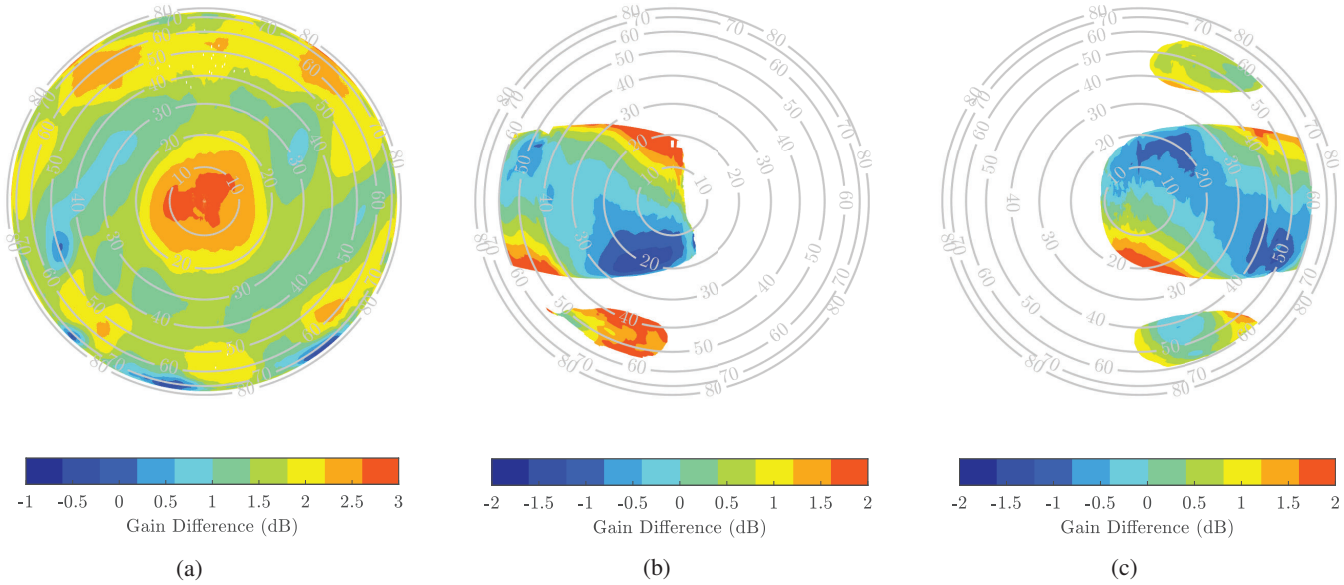



Fig. 1: Example FM07 antenna gain difference levels computed as $G_{updated} - G_{existing}$ (a) Zenith (b) Port (c) Starboard

by an analysis of a 5 year CYGNSS $\Gamma_{LR}$ record. This is complemented with tests of the constellation's 'self consistency' that are more independent of reference geophysical datasets or the properties of the surfaces observed in Section V. This is then followed by final conclusions and discussions in Section VI.

## II. Background

To maintain a healthy power budget, each CYGNSS flight model undertakes commanded roll maneuvers that are intended to maximize the exposure of their solar panels to sunlight. During these periods nominal science operations continue such that the constellation provides both 'non-rolled' and 'rolled' measurements using their zenith antennas that are used to track Global Positioning System (GPS) Effective Isotropic Radiated Power (EIRP) in real-time as well as their port and starboard nadir antenna modules that are intended to track specular reflections off the Earth's surface. The observation geometry properties in differing roll states were shown in Parts I [21] and II [22] to be instrumental in both identifying potential mischaracterizations in existing estimates of these patterns, highlighting the relationship these may have with Level-1 calibration artifacts impacting observables and ultimately with developing procedures intended to improve characterizations of in-orbit antenna patterns across all channels.

An illustrative example of how the updated patterns compare to preceding estimates for FM07's three antennas is illustrated in Fig. 1. Simple gain bias, that is a constant offset across the complete polar space between different sets of patterns, is not expected to compromise the calibration quality of observables. Instead, this would have the effect of shifting the means of observables by a factor commensurate with the gain offset. Conversely, it is the form of non-uniform differences that are depicted in Fig. 1 that are expected to have a more significant impact on calibration quality as it may increase or decrease the variance of measurements depending on how representative the patterns are of 'true' in-orbit behaviors.

In the case of FM07, for each of the antennas, updated estimates would suggest that true in-orbit gain levels are either ≈2 dB lower than previously thought or more than ≈3 dB higher compared to preceding characterizations depending on the subset of polar co-ordinates where a specular measurement maps. Part I [21] presented methodologies applicable for the constellation's zenith (direct signal) channels while those in Part II [22] are concerned with nadir antennas. The analyses presented in what follows contrast observables' behaviors using a Level-1 calibration scheme that incorporates the updated patterns with one that relies on preceding estimates. The results make clear that updated characterizations of antenna patterns are more representative of in-orbit levels.

## III. Observed Ocean Trends

Given the correspondence measurement incidence angles have to distinct polar subsets within the respective antenna patterns, it is of interest to assess NBRCS anomalies $\tilde{\sigma}_0(\theta_i, \varphi_r)$

$$\tilde{\sigma}_0(\theta_i, \varphi_r) = \frac{\frac{100}{N_r}\sum_{i=1}^{N_r}\sigma^0(\theta_i, \varphi_r) - \frac{100}{N_0}\sum_{i=1}^{N_0}\sigma^0(\theta_i, 0)}{\frac{1}{N_0}\sum_{i=1}^{N_0}\sigma^0(\theta_i, 0)} \tag{1}$$

as a function of incidence angle $\theta_i$ and roll angle $\varphi_r$, with $N_r$ indicating the number of rolled measurements and $N_0$ indicating not-rolled measurements. Illustrative examples are depicted in Fig. 2 showing the impact of nadir antenna pattern mischaracterizations on roll specific NBRCS anomalies that can exceed $\pm 20\%$ depending on incidence angle, channel and roll angle. The examples in Fig. 2 also show the benefits of the updated patterns. Significant improvements are noted where the anomalies exhibit a reduced dependence on incidence angle and are typically less than 5%. Some residual calibration

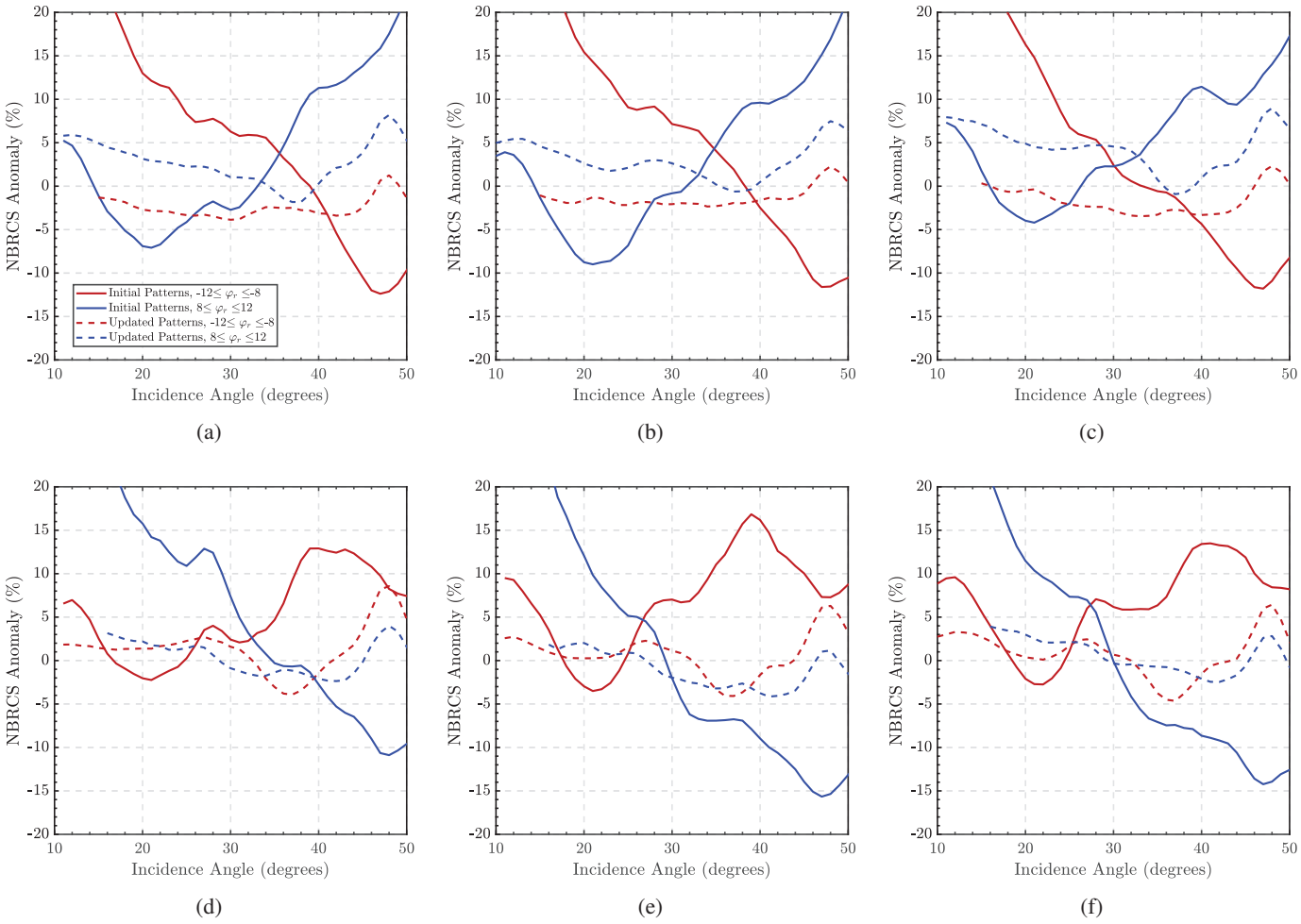



Fig. 2: NBRCS anomalies for observations with $6 \leq u_{10} \leq 8$ m/s ERA5 wind speeds at roll angles $\varphi_r = +10^\circ$ and $\varphi_r = -10^\circ$. View is limited to the range of incidence angles over which 90% of the measurements exist (a) FM02-Star (b) FM05-Star (c) FM07-Star (d) FM01-Port (e) FM04-Port (f) FM08-Port

TABLE I: The 90th percentile of NBRCS anomalies $|\overline{\sigma}_0|$ across all incidence angles contrasting NBRCS measurements recorded over surfaces whose ERA5 wind speed at the time and location of observation are in the range $6 \leq u_{10} \leq 8$ m/s across the roll angles $-8^\circ \leq \varphi_r \leq -12^\circ$ (i.e. -10°) and $8^\circ \leq \varphi_r \leq 12^\circ$ (i.e. +10°). All quoted values are in units of %. Entries are additionally binned by port-side antennas (P) and starboard-side antennas (S).

| $\varphi_r \downarrow$, ANT $\rightarrow$ | 1 P | 2 P | 3 P | 4 P | 5 P | 6 P | 7 P | 8 P | 1 S | 2 S | 3 S | 4 S | 5 S | 6 S | 7 S | 8 S |
|---|---|---|---|---|---|---|---|---|---|---|---|---|---|---|---|---|
| Prelaunch, -10 | 12.5 | 13.9 | 11.0 | 14.3 | 11.3 | 17.8 | 19.6 | 12.9 | 17.9 | 16.0 | 17.4 | 18.7 | 18.1 | 20.5 | 18.8 | 17.1 |
| Updated, -10 | 5.1 | 4.1 | 4.4 | 4.2 | 3.7 | 5.7 | 4.9 | 4.5 | 3.0 | 3.4 | 2.2 | 3.5 | 2.2 | 2.1 | 3.3 | 3.5 |
| Reduction | 59.0 | 70.3 | 60.0 | 70.9 | 67.6 | 67.8 | 75.1 | 64.9 | 83.1 | 78.6 | 87.1 | 81.2 | 88.0 | 89.9 | 82.5 | 79.5 |
| Prelaunch, +10 | 16.3 | 13.8 | 12.0 | 15.5 | 12.9 | 12.6 | 16.0 | 14.1 | 14.9 | 18.2 | 16.9 | 18.7 | 17.4 | 21.5 | 14.4 | 19.8 |
| Updated, +10 | 3.0 | 2.9 | 3.0 | 3.6 | 2.6 | 3.5 | 2.5 | 3.2 | 9.0 | 5.8 | 6.2 | 6.9 | 5.8 | 7.7 | 7.8 | 7.0 |
| Reduction | 81.7 | 79.2 | 75.3 | 76.8 | 79.6 | 72.3 | 84.3 | 77.5 | 39.4 | 67.9 | 63.3 | 62.9 | 66.5 | 64.4 | 45.8 | 64.6 |

uncertainties can still contribute anomalies that approach 8-9% at higher incidence angles (see Fig. 2(c)). As will be shown in what follows, the impact this has on other figures of merit appears minimal. Corresponding statistics capturing the 90th percentile $|\overline{\sigma}_0|$ (i.e. 90% of anomalies have a value less than that quoted in the table) are summarized in Table I. Anomaly reduction levels vary between 39.38-89.88% depending on the specific antenna and roll angle. Mean relative reductions of 71.53% and 72.64% occur for the port and starboard channels, respectively.

While similar trends are observed over other wind speed ranges, the choice to illustrate these effects using the subset of measurements occurring over ocean surfaces with $6 \leq u_{10} \leq 8$ m/s wind speeds is primarily motivated by considerations relating to measurement densities given the need to subset $\sigma^0$ by roll angle, flight model, antenna and incidence angle.

NBRCS statistics expressed as a function of reference ERA5 (European Centre for Medium-Range Weather Forecasts Re-

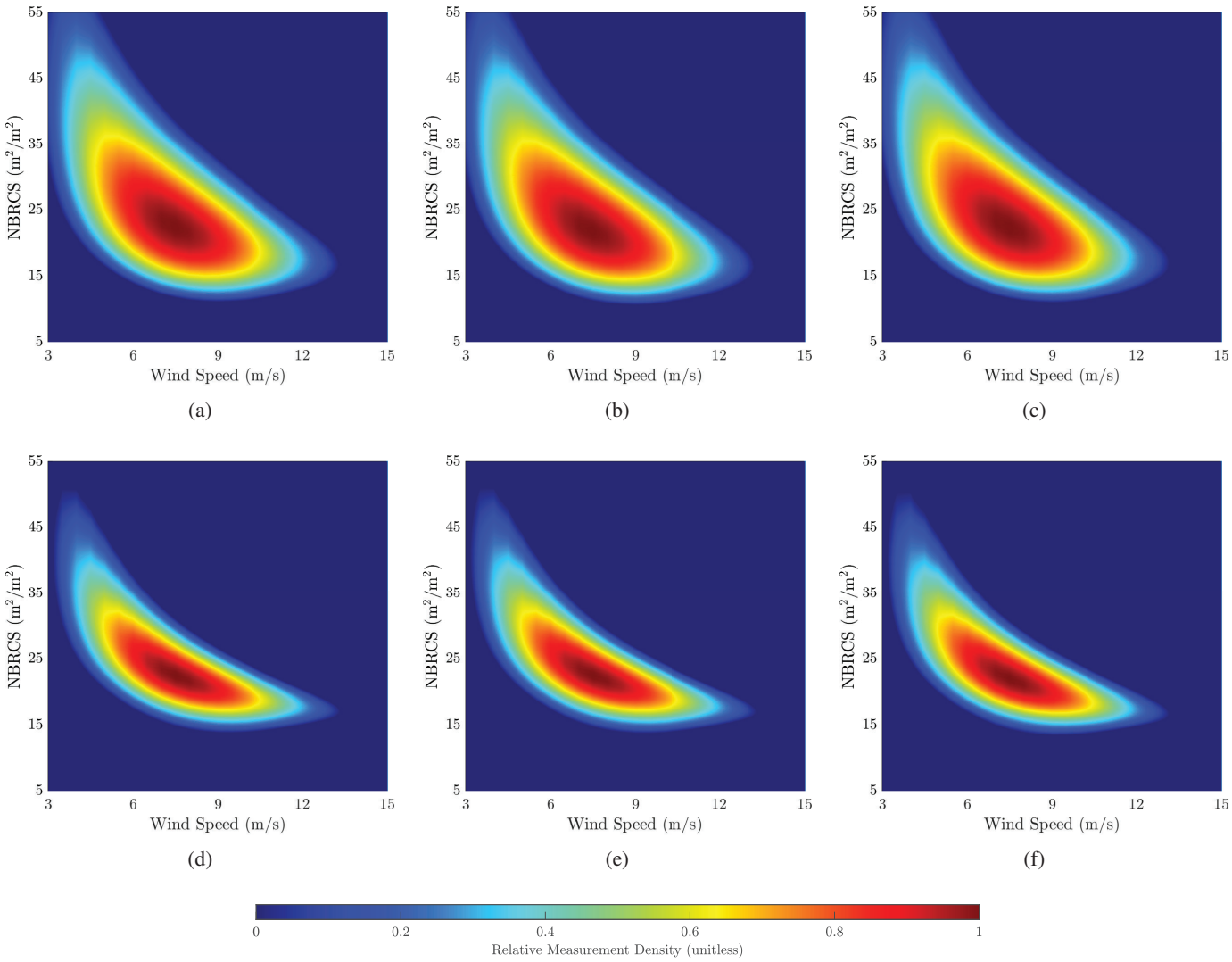



Fig. 3: Joint CYGNSS NBRCS, ERA5 winds speed PDFs. First row utilizes prelaunch patterns while second row highlights the impact of incorporating updated zenith and nadir antenna patterns. All other aspects of L1 calibration kept the same (a) FM02 (b) FM04 (c) FM06 (d) FM02 (e) FM04 (f) FM06

TABLE II: Mean NBRCS spread over the wind speed range $6 \leq u_{10} \leq 20$ m/s for Level-1 calibration algorithms that utilize initial prelaunch patterns compared to those incorporating updated patterns. Data from all incidence and roll angles is incorporated as part of this analysis. Entries are additionally binned by port-side antennas (P) and starboard-side antennas (S).

| **Version ↓, ANT →** | **1 P** | **2 P** | **3 P** | **4 P** | **5 P** | **6 P** | **7 P** | **8 P** | **1 S** | **2 S** | **3 S** | **4 S** | **5 S** | **6 S** | **7 S** | **8 S** |
|---|---|---|---|---|---|---|---|---|---|---|---|---|---|---|---|---|
| Initial (%) | 79.8 | 78.0 | 76.6 | 73.2 | 79.4 | 75.7 | 84.2 | 76.9 | 76.0 | 71.9 | 69.9 | 73.8 | 75.5 | 73.6 | 76.8 | 72.8 |
| Updated (%) | 47.3 | 45.9 | 47.0 | 46.5 | 46.5 | 48.4 | 47.9 | 46.3 | 49.3 | 47.9 | 48.2 | 48.3 | 48.1 | 51.3 | 48.2 | 47.5 |
| Reduction (%) | 40.8 | 41.1 | 38.6 | 36.5 | 41.4 | 36.0 | 43.2 | 39.8 | 35.1 | 33.4 | 31.0 | 34.6 | 36.2 | 30.2 | 37.2 | 34.7 |

TABLE III: Mean NBRCS uncertainty over the wind speed range $6 \leq u_{10} \leq 20$ m/s for Level-1 calibration algorithms that utilize initial prelaunch patterns compared to those incorporating updated patterns. Data from all incidence and roll angles is incorporated as part of this analysis. Entries are additionally binned by port-side antennas (P) and starboard-side antennas (S).

| **Version ↓, ANT →** | **1 P** | **2 P** | **3 P** | **4 P** | **5 P** | **6 P** | **7 P** | **8 P** | **1 S** | **2 S** | **3 S** | **4 S** | **5 S** | **6 S** | **7 S** | **8 S** |
|---|---|---|---|---|---|---|---|---|---|---|---|---|---|---|---|---|
| Initial (unitless) | 0.4 | 0.4 | 0.4 | 0.4 | 0.4 | 0.4 | 0.4 | 0.4 | 0.4 | 0.4 | 0.4 | 0.4 | 0.4 | 0.4 | 0.4 | 0.4 |
| Updated (unitless) | 0.2 | 0.2 | 0.2 | 0.2 | 0.2 | 0.2 | 0.2 | 0.2 | 0.3 | 0.3 | 0.3 | 0.3 | 0.3 | 0.3 | 0.3 | 0.3 |
| Reduction (%) | 40.5 | 39.5 | 38.1 | 37.9 | 39.2 | 33.3 | 41.3 | 37.6 | 27.9 | 36.2 | 31.1 | 32.0 | 36.7 | 29.2 | 36.5 | 36.5 |

analysis v5) winds were analyzed next. ERA5 reference winds are used as the main input for deriving CYGNSS's 'fully developed seas' (FDS) GMF (i.e. for tracks with lower winds that typically do not include storms). For an initial qualitative

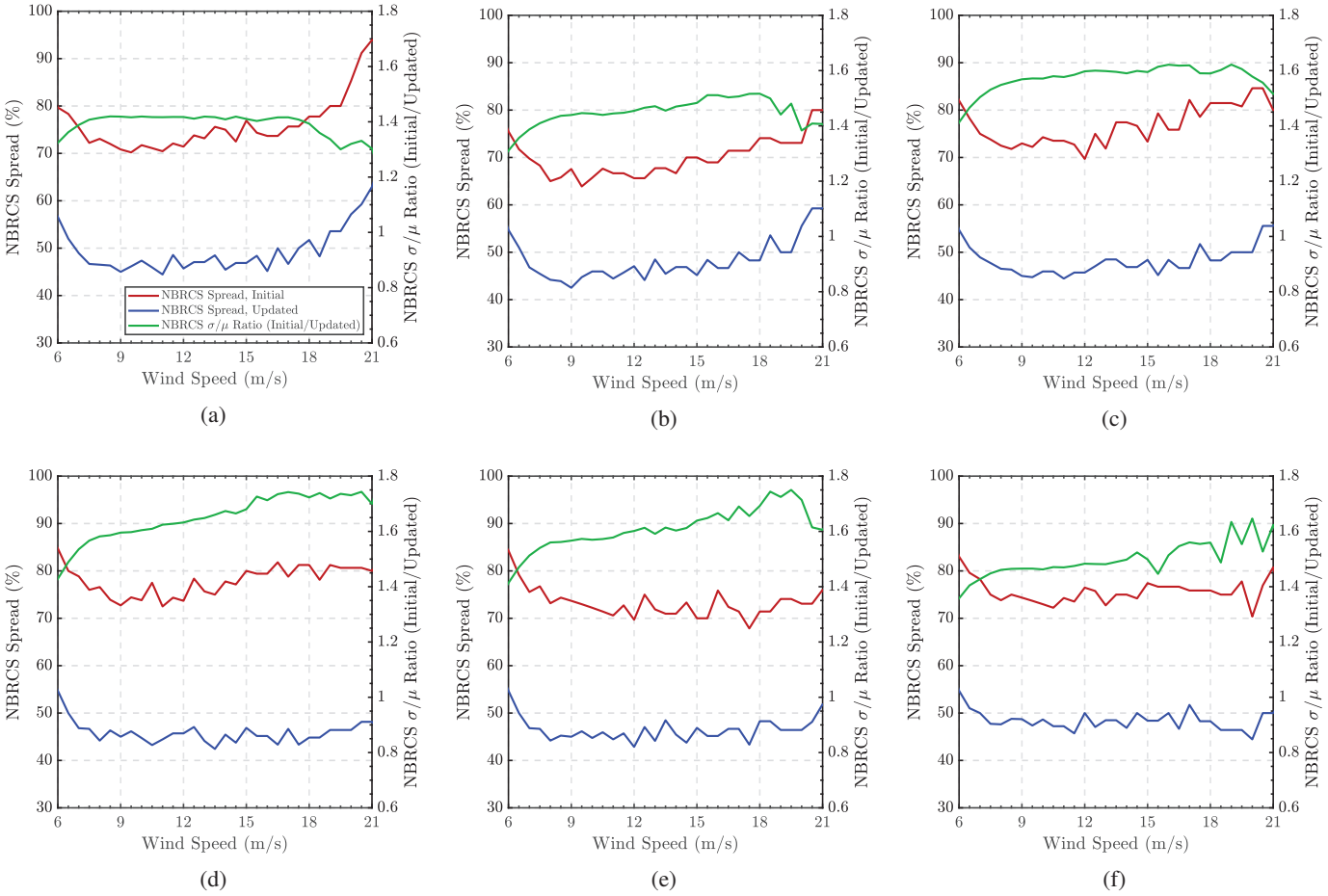



Fig. 4: CYGNSS NBRCS spread and uncertainty statistics expressed as a function of reference ERA5 wind speeds (a) FM01-Star (b) FM03-Star (c) FM07-Star (d) FM02-Port (e) FM04-Port (f) FM06-Port

assessment, example joint $\sigma^0 - u_{10}$ PDFs are depicted in Fig. 3, and illustrate behaviors that arise from a Level-1 calibration algorithm that utilizes initial patterns compared with that utilizing the updated patterns. This includes data from both nadir antennas on each of the example receivers, all incidence angles and all roll angles. While both sets of subplots indicate a declining NBRCS as a function of wind speed (a result of the associated increased roughening of the ocean surface), the appreciably higher uncertainties associated with 'initial NBRCS' in plots (a)-(c) is readily identifiable as evidenced by the increased spread of NBRCS across all wind speeds. Results with the updated patterns retain a similar physical behavior while reducing the variability in NBRCS estimates. The remaining spread in NBRCS at a given wind speed with the updated patterns can in large part be explained by variations in other properties of the ocean surface roughness not directly correlated with local wind speed, and are therefore not necessarily an indication of residual uncertainties in the antenna patterns. The extent of improvement in the patterns is described using two quantitative measures that include the initial uncertainty $\sigma_{initial}(u_{10})/\mu_{initial}(u_{10})$ relative to the updated uncertainty $\sigma_{updated}(u_{10})/\mu_{updated}(u_{10})$ as well as a spread metric $\upsilon$ (2) expressed as function of wind speed

$$\upsilon(u_{10}) = \frac{100 \cdot (\sigma_{90}(u_{10}) - \sigma_{10}(u_{10}))}{\sigma_{50}(u_{10})} \tag{2}$$

While the uncertainty measure, incorporating the NBRCS standard deviations $\sigma$ and means $\mu$, had been previously defined and utilized as a figure or merit [21], the spread measure aims to quantitatively describe the width of the NBRCS PDF at every wind speed by comparing the difference between the 90th ($\sigma_{90}$) percentile NBRCS to the 10th percentile NBRCS ($\sigma_{10}$) relative to the median NBRCS ($\sigma_{50}$) and therefore capturing the 'width' of the PDF and how repeatable a given NBRCS estimate at a prescribed wind speed is. The resulting trends for example port and starboard antennas are depicted in Fig. 4. While over the range $6 \leq u_{10} \leq 20$ m/s both metrics are observed to be weakly dependent on wind speed, it is observed that the uncertainties are considerably reduced across all example channels and wind speeds using the updated patterns. For example, in the case of FM01-starboard in plot (a), the mean spread is reduced by 40.8% approaching levels as low as 45% while the uncertainty is on average 100% higher using the initial patterns. Estimates of both across all channels are summarized in Tables II and III. The mean spread

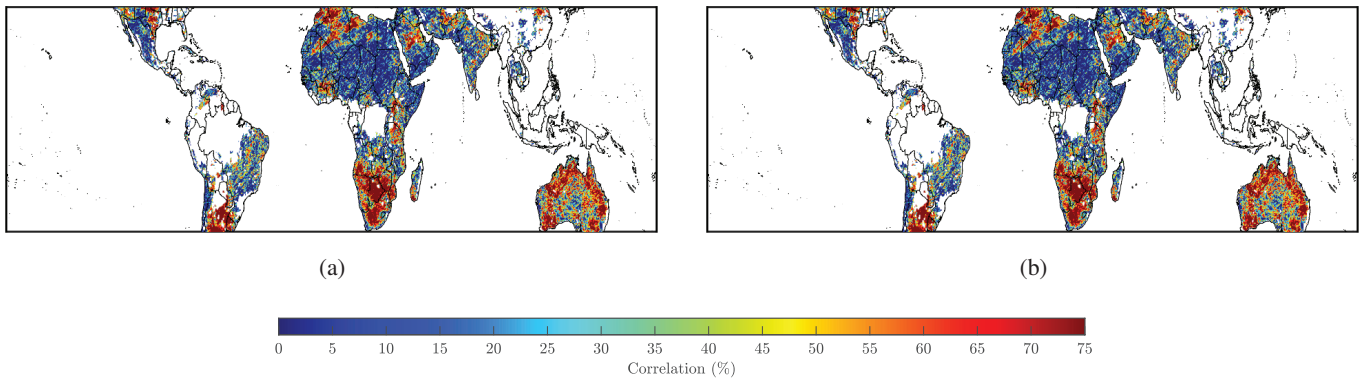



Fig. 5: CYGNSS reflectivity to SMAP soil moisture correlation map computed over a 31 day time series centered about March 1st, 2025. Regions where no correlation is reported are those flagged out by SMAP (a) Using prelaunch patterns (b) Using updated patterns

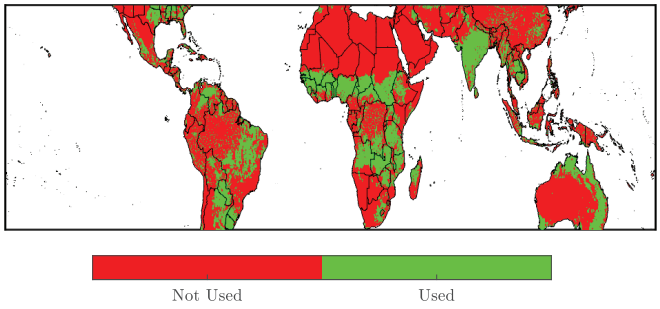



Fig. 6: Mask identifying pixels retained for use as part of further reflectivity correlation and uncertainty analysis

reduction is 36.86% and the mean uncertainty reduction is 35.83%.

## IV. Observed Land Trends

CYGNSS's land reflectivities have been used for sensing a variety of geophysical properties such as soil moisture ($m_v$), for which numerous retrieval algorithms have been proposed [3]–[6]. The reflectivities are derived from measured Level-1 delay Doppler Maps (DDMs), as the peak power that is later calibrated using a formulation that follows the Friis transmission equation. The mission's baseline retrieval approach [23] leverages the linear relationship between reflectivity, when expressed in decibels, and reference SMAP (Soil Moisture Active Passive) estimates to develop a site specific GMF and facilitate retrievals accordingly. It follows that a relevant figure of merit relates to assessing the impact of the updated patterns on CYGNSS reflectivity correlations to SMAP's reported soil moistures. An example of this reported on a 36 km Equal-Area Scalable Earth (EASE) grid is shown in Fig. 5. While the maps in plots (a) and (b) nominally amount to March 1st, 2025 correlation maps using initial and updated patterns, respectively, they are constructed using a 31 day time series of daily averaged CYGNSS reflectivities and SMAP soil moistures using +/-15 days about March 1st, 2025; the correlations are subsequently reported on a per-pixel basis. While it is instructive to examine the example maps in Fig. 5, reliance on these 'snapshot' correlation maps is found to be a highly unreliable indicator of relative correlation and reflectivity uncertainty differences, in the context of Level-1 calibration and validation activities. This is in part due to the fact that the two vary significantly depending on the day of year (DOY), specific regions and in particular their corresponding land covers along with level of soil moisture dynamics also varying in time and space. This motivated limiting comparisons to regions meeting prescribed conditions:

1) Soil moisture dynamics: It is well established that in dry regions such as the Middle East and North Africa (MENA) and significant transects of Australia exhibit highly limited soil moisture variability such that correlations of both CYGNSS reflectivity to SMAP's soil moisture and SMAP's soil moisture to in situ gauges are low. As a result differencing these low, and unrepresentative, measures gives rise to highly noisy estimates. Instead, an 8 year record of SMAP's soil moisture is used to interrogate dynamics while noting pixel specific differences in the 10th and 90th pixel specific percentiles of soil moisture as a measure of dynamics. Subsequently, the pixels that exhibit dynamics (i.e. differences in high and low soil moistures) that fall in the 50th percentile or greater are retained for further analysis.
2) Physical dependence: While the magnitude of measured reflectivities will undergo changes as a function of a variety of surface properties including texture, sand and clay fractions, bulk density, temperature, roughness, vegetation cover and the like its permittivity undergoes the largest increases as a function of its volumetric soil moisture content. In turn, this increases measured reflectivities such that a line whose slope is positive relating CYGNSS reflectivities and SMAP soil moistures is the expected physical relationship. Nonetheless, the confounding effects of other surface properties, inland water body contamination, interference and the like can cause some pixels to exhibit behaviors where the slope of the line of best fit relating the two approaches zero. Differences over corresponding regions similarly provides noisy figures of merit. A similar climatology was developed and only the regions whose reflectivity vs $m_v$ slope falls in the top 50th percentiles was used in subsequent analysis.
3) Correlation: Closely related is the fact that due to the

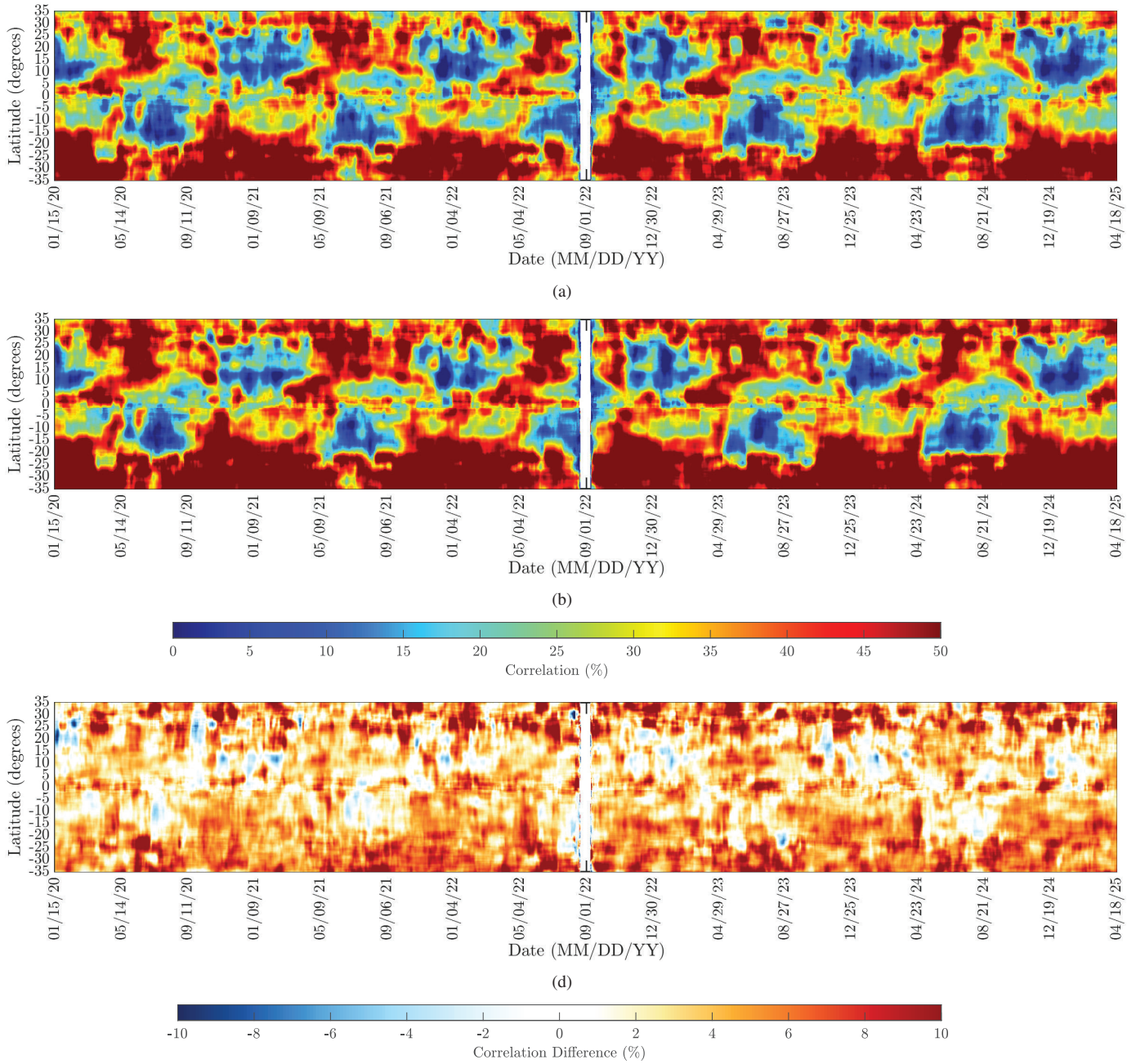



Fig. 7: CYGNSS reflectivity vs SMAP soil moisture correlation Hovmöller diagram (a) Using prelaunch patterns (b) Using updated patterns (c) Correlation difference computed as updated - initial (i.e. positive numbers indicate improvements)

impacts of the same confounding effects the extent of CYGNSS reflectivity correlations to SMAP's soil moistures is also highly varied such that a further requirement is placed for pixels to be used, their reflectivity/soil moisture correlations must also fall in the top 50th percentiles.

For a pixel to be retained for further assessments, all three conditions were enforced resulting in the mask depicted in Fig. 6. Only reference soil moistures that SMAP identifies as being of recommended quality are used in this analysis. This analysis is intended to test not the superiority of one instrument compared to another for the sensing of soil moisture but rather selects pixels that will be most useful in assessing the impacts of various calibration schemes in terms of observables' sensitivity to soil moisture. Subsequently, for every DOY over the period January 2020 to August 2025 a 31 day time series (+/- 15 days centered about 'current DOY') is constructed and a corresponding 'daily' correlation map is produced. The mask in Fig. 6 is then applied and each of the daily correlation maps is then averaged along longitude and used to develop the latitude-time Hovmöller diagrams in Fig. 7. The process is repeated using both initial and updated tables with the corresponding trends captured in plots (a) and (b) respectively. These Hovmöller diagrams provide

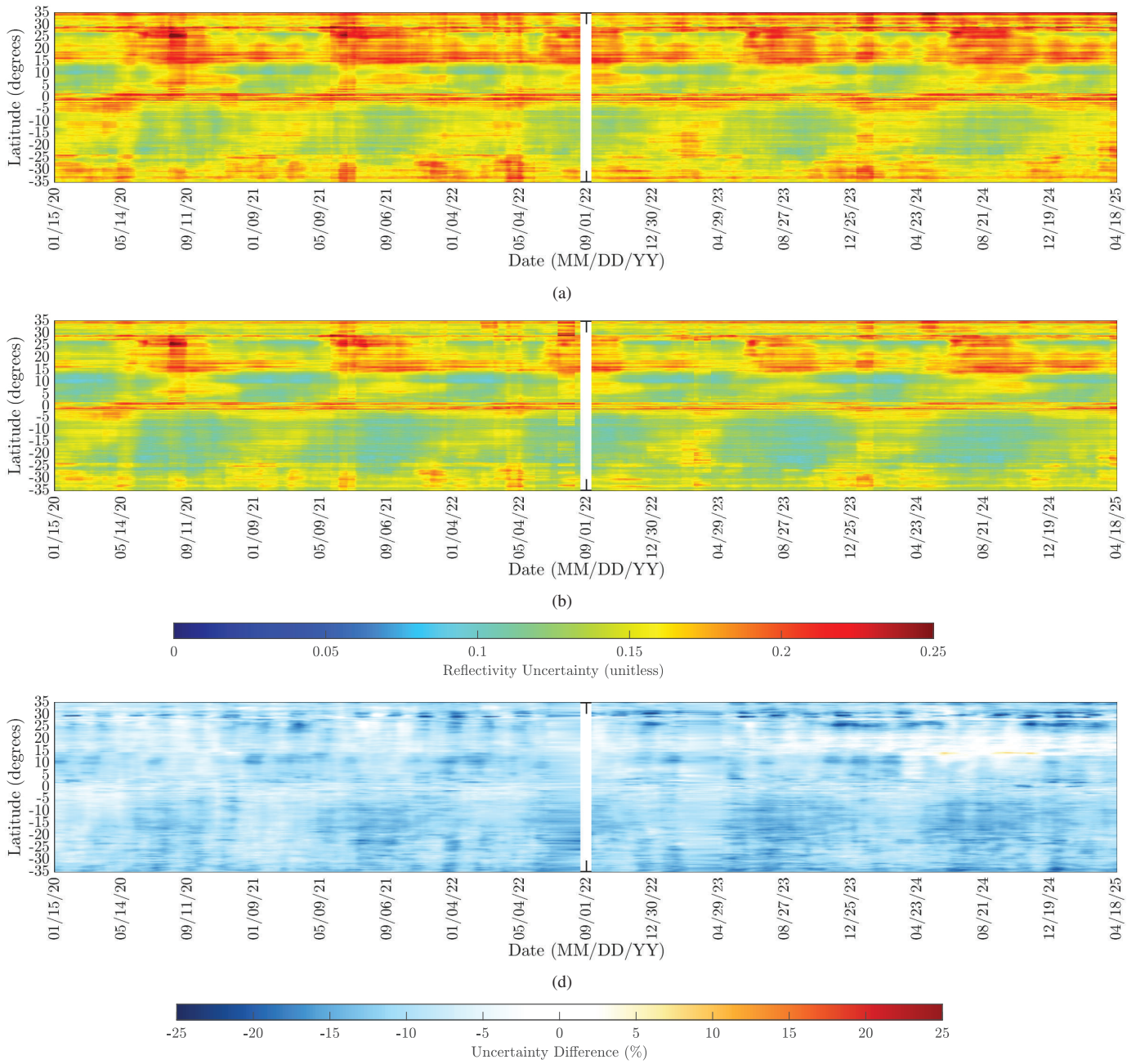



Fig. 8: CYGNSS reflectivity uncertainty Hovmöller diagram (a) Using prelaunch patterns (b) Using updated patterns (c) Uncertainty difference computed as updated - initial (i.e. negative numbers indicate improvements)

a more comprehensive, and succinct, summary of behaviors across both space and time. Additionally, the temporal trends in Fig. 7 are directly related to hemispheric seasonal soil moisture dynamics. For example, the diagonal structure of higher correlation beginning at the equator on March 2020 and traversing North over a period of ≈4 months while repeating year-to-year coincides with periods where reference SMAP soil moistures undergoes more significant changes that are typically on the order of 0.2-0.25 $m^3/m^3$. Similar effects are also noted in the southern hemisphere albeit phase shifted in time given contrasting seasonality. It follows that periods exhibiting reduced correlations are also associated with lower soil moisture variability, analysis of which suggests changes on the order of $\Delta m_v \leq 0.15$ $m^3/m^3$.

A similar process is applied to assess the differences in uncertainty, expressed in terms of the ratio of reflectivity standard deviation relative to the mean, resulting in the uncertainty Hovmöller diagrams in Fig. 8. Similar seasonal trends are also observed where in periods exhibiting lower soil moisture dynamics, a higher level of reflectivity uncertainty is noted. Nonetheless, an initial visual assessment of plots (a) and (b), utilizing initial and updated patterns respectively, highlights the higher mean level of uncertainty associated with the use of prelaunch patterns.

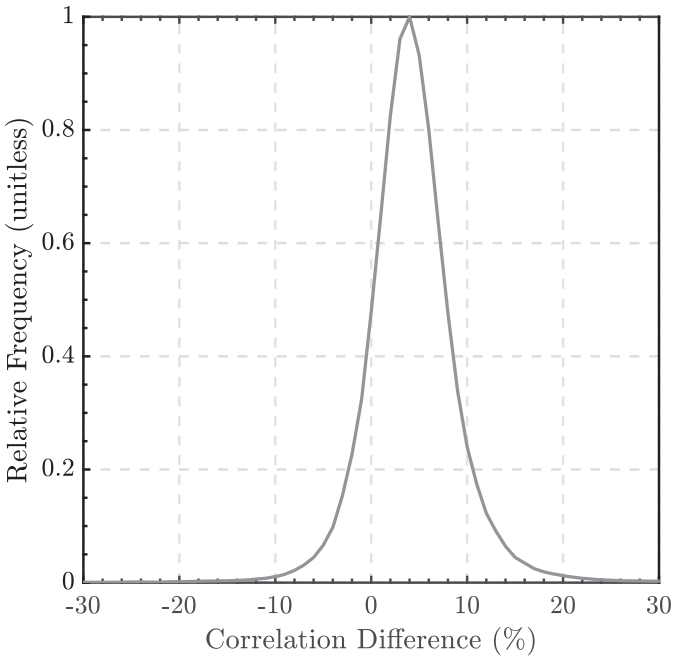



Fig. 9: PDF summarizing correlation differences using respective Hovmöller diagrams. Differences computed as correlation obtained when using updated patterns compared to those achieved when using prelaunch patterns. Positive numbers indicate improvement.

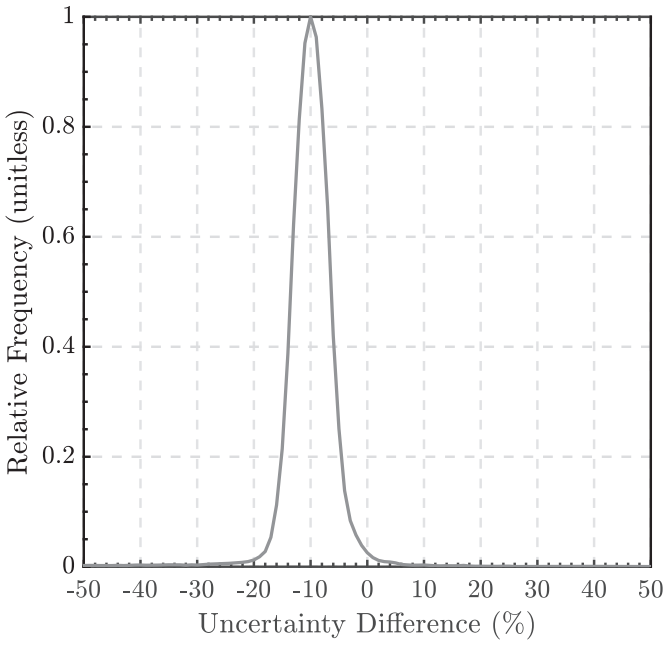



Fig. 10: PDF summarizing uncertainty differences using respective Hovmöller diagrams. Differences computed as the uncertainty obtained when using updated patterns compared to those achieved when using prelaunch patterns. Negative numbers indicate improvement.

Subsequently, to further assess the impact of the updated patterns, the correlation difference PDF in Fig. 9 is generated by differencing Fig. 7(a) and (b). It is assessed that the updated patterns improve reflectivity correlations to SMAP's soil moisture across 83.14% of the entries assessed with a mean increase of 4.06% globally, with some regions exhibiting correlation increases $\geq 20\%$. Greater increases appear to be less dependent on specific land-covers and instead appear to be related to soil moisture variability where for areas experiencing higher levels of dynamics within the duration of a given time series, larger improvements are observed. This is also done in Fig. 10 where it is observed that uncertainties are reduced using the updated tables across 98% of the entries analyzed with a mean reduction of 10%.

It is also noted that the along-time 'stripes' that appear in Fig. 7 and Fig. 8 at latitude $\approx 0^\circ$ are a consequence of there being very few longitudinal pixels available for analysis near the equator (see Fig. 6) as opposed to the feature being telling of distinct CYGNSS behaviors in those regions.

## V. Constellation Self Consistency

The use of a 'distributed' observation architecture where a total of 16 physical receive nadir antennas, each with its own set of calibration biases, along with a wide range of transmitters as is the case with GNSS-R observations increases the likelihood of varied errors impacting their measurements. Additionally, while the preceding assessments were informed by independent reference geophysical datasets it is also instructive to explore the impact of the updated patterns on observable quality irrespective of the geophysical properties of the surface at the time of observation. A relevant test of the effectiveness with which such errors are accounted for entails exploring the 'self consistency' of CYGNSS observables using colocations across different receive pairs over spatial and temporal colocation windows where surface properties can be assumed to be constant. Importantly, this makes no assumptions regarding the properties of the surface and therefore circumvents related uncertainties. An example of this is shown in Fig. 11 where plot (a) reports the joint PDF of NBRCS colocated pairs over a 25 km footprint and 15 minute separation using the initial patterns. This facilitates 1.063 million colocated pairs. The same analysis is repeated in plot (b) using the updated patterns. This includes measurements made across all roll states, surface wind speeds and observation geometries using an identical population of measurements. Given the physical dependence of $\sigma^0$ on incidence angle, only colocations arising from different antennas across different receivers whose incidence angles differ by $\theta_i \leq 3^\circ$ are retained. In both cases, it is observed that colocations are highly correlated and are centered near the 1-1 line. In the case of plot (a) correlation is $\approx 78.28\%$; using the updated patterns in plot (b) correlation increases to 87.14%. Importantly, as a result of the various mischaracterizations of zenith and nadir antenna patterns the overall variability of NBRCS estimates that utilize prelaunch patterns are considerably higher as evidenced by the increased 'spread' about the 1-1 line. The uRMSE is 21.38 $m^2/m^2$ in plot (a) whereas it is 12.99 $m^2/m^2$ in plot (b). Closely related is the fact that the range of NBRCS difference across colocated pairs is reduced from 4.23 $m^2/m^2$ to 1.97 $m^2/m^2$ on average.

The geophysical properties over land vary on longer time scales such that the temporal window colocation used in the analysis in Fig. 12 is 24 hours. In contrast to analysis

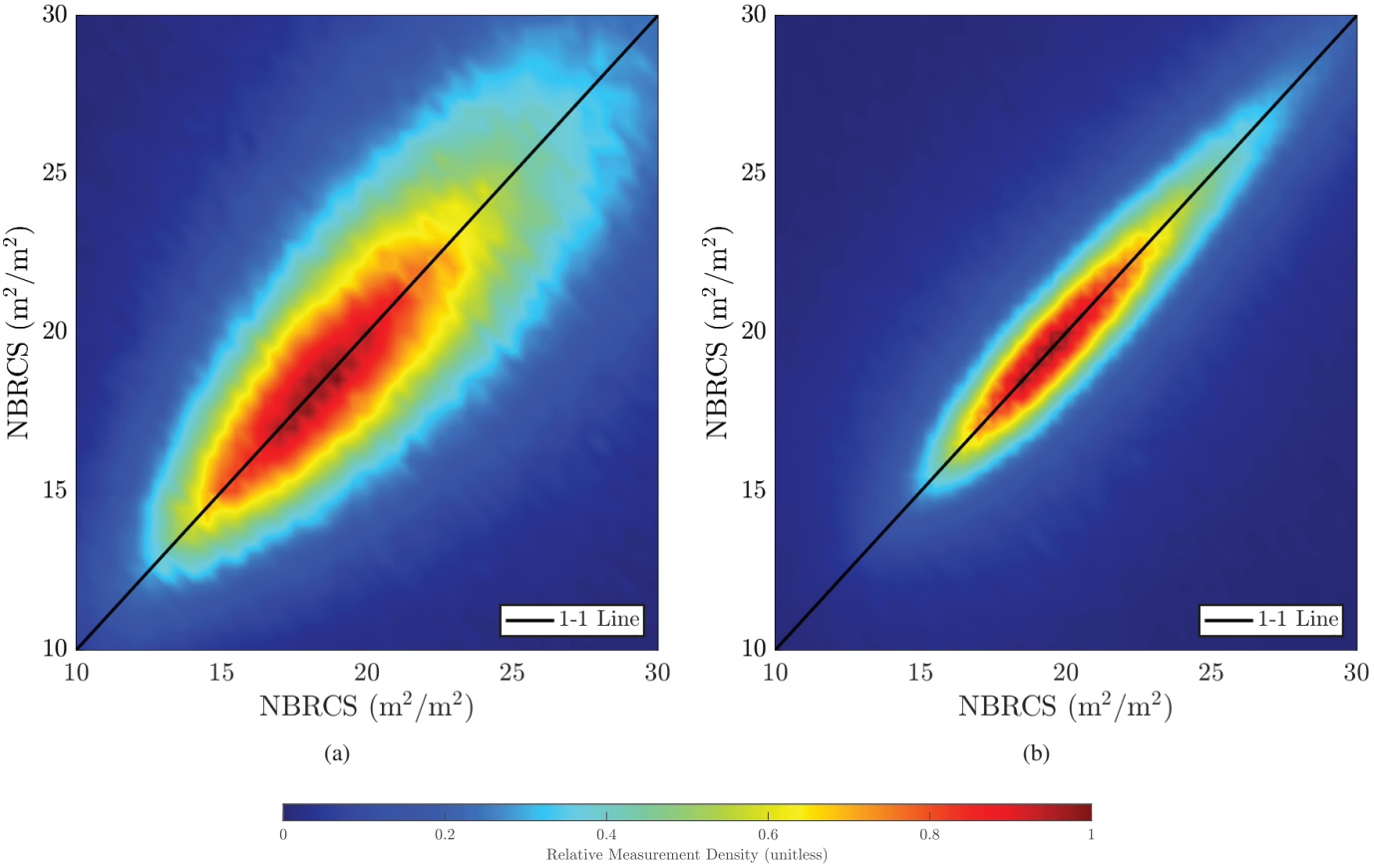



Fig. 11: Ocean NBRCS colocation PDFs generated over a 25 km and 15 minute window. The PDFs are 'generalized' in that the x-axis and y-axis do not correspond to specific receive channels, instead colocated pairs always arise from unique antennas (i.e. self colocation is excluded) (a) Using prelaunch patterns (b) Using updated patterns

of the ocean surface however, the heterogeneous nature of land measurements motivates selecting a finer 3 km spatial colocation window. Together, these conditions provide 49049 colocated reflectivity estimates for analysis. Similar trends are also observed where reported estimates are highly consistent across a wide range of reflectivities. In the case of land reflectivities, the RMSD is reduced from 3.35 dB to 3.09 dB while the correlation increases from 88.01% to 89.09%. The range of reflectivity difference across colocated pairs is reduced from 1.55 dB to 1.23 dB on average.

## VI. Conclusion

Accurate reconstruction of in-orbit direct (zenith) and reflected (nadir) signal channel antenna patterns is crucial for enhancing observables' correspondence to geophysical properties of interest and reducing related Level-1 calibration discrepancies. While pre-launch ground based characterizations can alleviate some of these uncertainties, the costs associated with fully testing spacecraft flight models (FMs) may be prohibitive and may often inadequately capture in-orbit behaviors given the thermal, mechanical and electromagnetic effects receivers are impacted by once deployed into Low Earth Orbit (LEO), all leading to departures from nominal behaviors.

Over this three part series, the utility of in-orbit roll maneuvers for enhancing calibration quality through improved in-orbit pattern characterization was demonstrated. To maintain a healthy power budget, each CYGNSS flight model undertakes commanded roll maneuvers that are intended to maximize the exposure of their solar panels to sunlight. During these periods nominal science operations continue such that the constellation provides both 'non-rolled' and 'rolled' measurements using their zenith antennas that are used to track Global Positioning System (GPS) Effective Isotropic Radiated Power (EIRP) in real-time as well as their port and starboard nadir antenna modules that are intended to track specular reflections off the Earth's surface.

In Parts I and II it was shown that this gives rise to distinct measurement properties (unavailable for non-rolled data) that were leveraged as part of the proposed techniques to reconstruct the receivers' zenith antenna patterns, nadir antenna patterns and gain patterns across every GPS transmitter whose reflections were tracked by CYGNSS. In the case of the direct channel, this is in part facilitated by the fact that the roll maneuvers give rise to EIRP measurements with multiple off-boresight angles at a fixed polar co-ordinate in the receivers' patterns. In an analogous fashion, the roll maneuvers give rise to measurements taken at multiple incidence angles at a fixed polar co-ordinate in the receivers' nadir antenna patterns. It is instructive to emphasize that for 'non-rolled' datasets, it is typically the case that for a given receiver/transmitter pairing measurements occur at one (or over a limited range) of off-

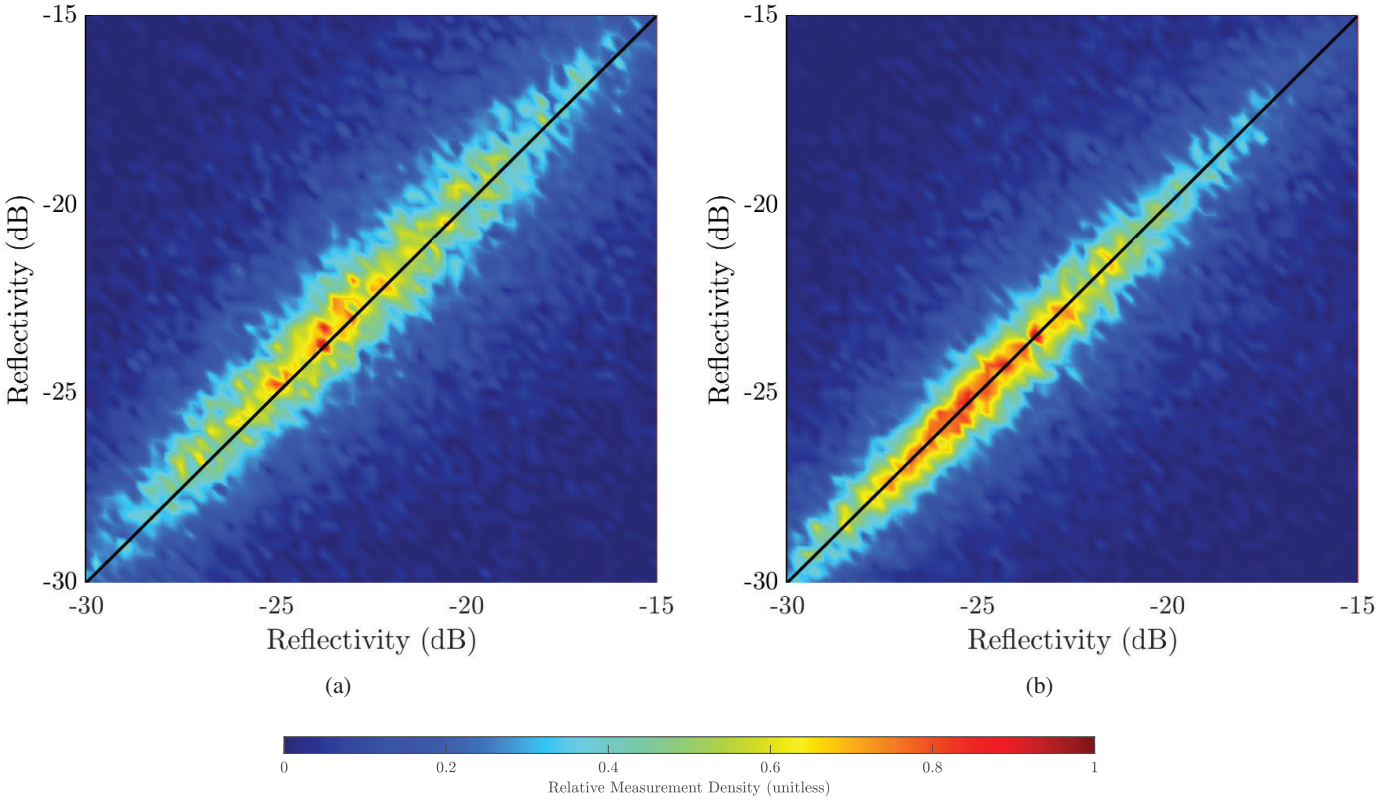



Fig. 12: Land reflectivity colocation PDFs generated over a 3 km and 24 hour window. The PDFs are 'generalized' in that the x-axis and y-axis do not correspond to specific receive channels, instead colocated pairs always arise from unique antennas (i.e. self colocation is excluded) (a) Using prelaunch patterns (b) Using updated patterns

boresight and incidence angle given a fixed body azimuth and elevation co-ordinate.

For direct channel activities, the proposed technique led to non-uniform corrections to the CYGNSS zenith antenna patterns by up to 4 dB relative to prior estimates. Uncertainties in the Effective Isotropic Radiated Power (EIRP) of the GPS transmissions are reduced by an average of 33%. The calibration improvements highlight the efficacy of leveraging 'rolled data' for deriving GPS transmitter patterns as well as demonstrating that data records as short as a single day can be used with as little as 4% uncertainty in the resulting improvement. Several practical considerations were also provided to operators of other existing and future GNSS-R payloads. This included demonstrating that in spite of the 'coupled' nature of multiple EIRP calibration terms, the use of the proposed methodologies does not require the implementation of an iterative scheme thereby significantly enhancing their computational efficiency. Additionally, it was demonstrated that as few as 100 measurements per off-boresight angle increment were sufficient to estimate a representative GPS pattern such that for a receiver operating with a duty cycle comparable to CYGNSS, a single day of data would be sufficient to accumulate the necessary number of measurements. For a more comprehensive overview, see Part I.

For reflected channel activities, it was shown in Part II that the updated gain estimates differ by -3 to 3 dB in a non-uniform fashion. In this Part III, the impact of incorporating the updated patterns into the mission's standard Level-1 calibration of NBRCS and reflectivity was explored. It was shown that NBRCS anomalies related to antenna pattern uncertainties are reduced by an average of ≈70% while overall variability as a function of ERA5 reference wind speeds is reduced by an average of ≈36%. Efficacy of the calibration improvements applied to land reflectivity is assessed using reference SMAP soil moisture estimates. The results suggest improvements impacting over 83.14% of measurements, by an average of 4.06% while reducing uncertainty by a mean of 10% across 98% of all observations. The findings presented across this three part series highlight the utility of in-orbit roll maneuvers for the improved calibration of Level-1 GNSS-R observables. Several relevant practical considerations were also provided to operators of other existing and future GNSS-R payloads. For example, the operators of future GNSS-R instruments may be limited in terms of the number of roll angles they may be able to maneuver their flight models into due to mechanical constraints or due to other considerations relating to the interruptions this may cause to their routine science operations. As such, it was of interest to explore the minimum number of roll angles needed to pursue the prescribed procedures. It was shown that a minimum of collections at three roll angles would likely be required. Other studies of the minimum number of measurements required for a given body elevation and azimuth angle showed that as few as 100 measurements per pixel at these multiple roll angles would be sufficient. For a more comprehensive overview, see Part II.

Finally, it is also noted that analysis of the properties of

CYGNSS's observations across varied roll maneuvers suggests that they present numerous avenues for the improved calibration of GNSS-R observables. It follows that the methodologies overviewed in this work constitute a limited subset of a wider range of techniques that can be leveraged for the improvement of GNSS-R system calibration quality more generally.

## REFERENCES


[1] R. Balasubramaniam and C. Ruf, "Characterization of rain impact on L-Band GNSS-R ocean surface measurements," *Remote Sensing of Environment*, vol. 239, p. 111607, Mar. 2020, doi: https://doi.org/10.1016/j.rse.2019.111607.

[2] R. Balasubramaniam and C. S. Ruf, "The Impact of Rain on L1 GNSS-R Radar Scattering Cross-Section," *International Geoscience and Remote Sensing Symposium*, pp. 7900–7903, Jul. 2019, doi: https://doi.org/10.1109/igarss.2019.8900302.

[3] L. J. Wernicke, C. C. Chew, and E. E. Small, "Spatially Interpolated CYGNSS Data Improve Downscaled 3 km SMAP/CYGNSS Soil Moisture," *Remote Sensing*, vol. 16, no. 16, pp. 2924–2924, Aug. 2024, doi: https://doi.org/10.3390/rs16162924.

[4] O. Eroglu, M. Kurum, D. Boyd, and A. C. Gurbuz, "High Spatio-Temporal Resolution CYGNSS Soil Moisture Estimates Using Artificial Neural Networks," *Remote Sensing*, vol. 11, no. 19, p. 2272, Sep. 2019, doi: https://doi.org/10.3390/rs11192272.

[5] M. P. Clarizia, N. Pierdicca, F. Costantini, and N. Floury, "Analysis of CYGNSS Data for Soil Moisture Retrieval," *IEEE Journal of Selected Topics in Applied Earth Observations and Remote Sensing*, vol. 12, no. 7, pp. 2227–2235, Jul. 2019, doi: https://doi.org/10.1109/jstars.2019.2895510.

[6] S. H. Yueh, R. Shah, M. J. Chaubell, A. Hayashi, X. Xu, and A. Colliander, "A Semiempirical Modeling of Soil Moisture, Vegetation, and Surface Roughness Impact on CYGNSS Reflectometry Data," *IEEE Transactions on Geoscience and Remote Sensing*, pp. 1–17, 2020, doi: https://doi.org/10.1109/tgrs.2020.3035989.

[7] H. Carreno-Luengo, G. Luzi and M. Crosetto, "Above-Ground Biomass Retrieval over Tropical Forests: A Novel GNSS-R Approach with CyGNSS," *Remote Sensing*, vol. 12, no. 9, p. 1368, 2020, doi: https://doi.org/10.3390/rs12091368.

[8] Milad Asgarimehr, D. Entekhabi, and A. Camps, "Diurnal Vegetation Moisture Cycle in the Amazon and Response to Water Stress," *Geophysical Research Letters*, vol. 51, no. 19, Oct. 2024, doi: https://doi.org/10.1029/2024gl111462.

[9] M. Morris, C. Chew, J. T. Reager, R. Shah and C. Zuffada, "A Novel Approach To Monitoring Wetland Dynamics Using CYGNSS: Everglades Case Study," *Remote Sensing of Environment*, 2019, doi: https://doi.org/10.1016/j.rse.2019.111417.

[10] C. Ruf et al., "Characterization of CYGNSS Ocean Surface Wind Speed Products," *Remote Sensing*, vol. 16, no. 22, pp. 4341–4341, Nov. 2024, doi: https://doi.org/10.3390/rs16224341.

[11] A. M. Warnock, C. S. Ruf, A. Russel, M. M. Al-Khaldi, and R. Balasubramaniam, "CYGNSS Level 3 Merged Wind Speed Data Product for Storm Force and Surrounding Environmental Winds," *IEEE Journal of Selected Topics in Applied Earth Observations and Remote Sensing*, vol. 17, pp. 6189–6200, Jan. 2024, doi: https://doi.org/10.1109/jstars.2024.3379934.

[12] A. Warnock and C. Ruf, "Response to Variations in River Flowrate by a Spaceborne GNSS-R River Width Estimator," *Remote Sensing*, vol. 11, no. 20, p. 2450, 2019, doi: https://doi.org/10.3390/rs11202450.

[13] J. Zhang and Y. Jade Morton, "Inland Water Body Surface Height Retrievals Using CYGNSS Delay Doppler Maps," *IEEE Transactions on Geoscience and Remote Sensing*, vol. 61, pp. 1–16, Jan. 2023, doi: https://doi.org/10.1109/TGRS.2023.3330410.

[14] J. Mashburn, P. Axelrad, C. Zuffada, E. Loria, A. O'Brien, and B. Haines, "Improved GNSS-R Ocean Surface Altimetry With CYGNSS in the Seas of Indonesia," *IEEE Transactions on Geoscience and Remote Sensing*, vol. 58, no. 9, pp. 6071–6087, Sep. 2020, doi: https://doi.org/10.1109/TGRS.2020.2973079.

[15] H. M. J. P. Barre, B. Duesmann and Y. H. Kerr, "SMOS: The Mission and the System," *IEEE Transactions on Geoscience and Remote Sensing*, vol. 46, no. 3, pp. 587–593, Feb. 2008, doi: https://doi.org/10.1109/tgrs.2008.916264.

[16] P. S. Narvekar, D. Entekhabi, S. B. Kim, and E. G. Njoku, "Soil Moisture Retrieval Using L-Band Radar Observations," *IEEE Transactions on Geoscience and Remote Sensing*, vol. 53, no. 6, pp. 3492–3506, Jan. 2015, doi: https://doi.org/10.1109/tgrs.2014.2377714.

[17] S. H. Yueh and J. Chaubell, "Sea Surface Salinity and Wind Retrieval Using Combined Passive and Active L-Band Microwave Observations," *IEEE Transactions on Geoscience and Remote Sensing*, vol. 50, no. 4, pp. 1022–1032, Apr. 2012, doi: https://doi.org/10.1109/tgrs.2011.2165075.

[18] P. Rosen et al., "The NASA-ISRO SAR mission - An international space partnership for science and societal benefit," *IEEE Radar Conference*, May 2015, doi: https://doi.org/10.1109/radar.2015.7131255.

[19] D. Petrolati et al., "An Overview of the Copernicus Rose-L SAR Instrument," Jul. 2023, doi: https://doi.org/10.1109/igarss52108.2023.10281670.

[20] C. Ruf, D. McKague, D. Posselt, S. Gleason, M.P. Clarizia, V. Zavorotny, T. Butler, J. Redfern, W. Wells, M. Morris, J. Crespo, C. Chew, E. Small, D. Pasqual, T. Wang, A. Warnock, D. Mayers, M. Al-Khaldi, A. J. O'Brien, "CYGNSS Handbook (2nd ed.)," Michigan Publishing Services, Ann Arbor, MI, ISBN 978-1-60785-549-1.

[21] M. M. Al-Khaldi, S. Gleason, C. Ruf, J. T. Johnson, D. S. McKague, A. Russel, W. L. Wells, T. Wang, D. Twigg, P. McEnaney and J. Synowiec, "Utilizing In-Orbit CYGNSS Roll Maneuvers For Improved Level-1 Calibration - Part I: Application To Direct Signal Channels," *IEEE Transactions on Geoscience and Remote Sensing*, 2026.

[22] M. M. Al-Khaldi, S. Gleason, C. Ruf, J. T. Johnson, D. S. McKague, A. Russel, W. L. Wells, T. Wang, D. Twigg, P. McEnaney and J. Synowiec, "Utilizing In-Orbit CYGNSS Roll Maneuvers For Improved Level-1 Calibration - Part II: Application To Reflected Signal Channels," *IEEE Transactions on Geoscience and Remote Sensing*, 2026, Under Review.

[23] C. Chew and E. Small, "Description of the UCAR/CU Soil Moisture Product," *Remote Sensing*, vol. 12, no. 10, p. 1558, May 2020, doi: https://doi.org/10.3390/rs12101558.




**Mohammad M. Al-Khaldi** received the bachelor's degree in electrical engineering from the American University of Sharjah, Sharjah, United Arab Emirates, in 2015, the M.S. degree in electrical engineering from Texas A&M University, College Station, TX, USA, in 2017, and the M.S. degree in electrical and computer engineering from The Ohio State University, Columbus, OH, USA, in 2019, where he completed his Ph.D. degree with the Department of Electrical and Computer Engineering and ElectroScience Laboratory in 2020. Dr. Al-Khaldi was previously a Project Scientist I, Post-doctoral Fellow II and Post-doctoral Fellow I at the University Corporation for Atmospheric Research's (UCAR's) COSMIC Program in Boulder, CO, USA. He is currently a Research Scientist at The Ohio State University's ElectroScience Laboratory and Department of Electrical and Computer Engineering.

Dr. Al-Khaldi has been a member of the NASA CYGNSS mission science team, NASA CYGNSS mission calibration and validation team, NASA GNSS science team, IEEE GRSS Technical Committee on Modeling in Remote Sensing, IEEE GRSS Technical Committees on Frequency Allocations in Remote Sensing, has been an associate member of commissions B and F of the International Union of Radio Science (URSI), has been the NASA CSDA GNSS-R Subject Matter Expert (SME) and served as an Associate Editor of Radio Science as well as a Topical Associate Editor for the IEEE Transactions on Geoscience and Remote Sensing.

His current research interests include applied electromagnetics, rough surface scattering, and spaceborne remote sensing.



**Scott Gleason** received the B.S. degree in electrical and computer engineering from the State University of New York at Buffalo, Buffalo, NY,USA, the M.S. degree in engineering from Stanford University, Stanford, CA, USA, and the Ph.D. degree in applied physics from the University of Surrey, Surrey, U.K., in 1991, 1999 and 2007, respectively. He is currently the President of the Daaxa LLC consulting company, specializing in GNSS instruments, calibration and remote sensing applications. He is a Co-Investigator on the science team and Instrument Scientist for the NASA CYGNSS mission. He has worked in the areas of astronautics, remote sensing and global navigation satellite systems for more than 20 years, including at NASAs Goddard Space Flight Center, Stanford's GPS Laboratory, Surrey Satellite Technology Limited, Concordia University (Montreal, Canada), Southwest Research Institute, the University Corporation for Atmospheric Research and the National Oceanography Centre, Southampton, U.K.



**Christopher S. Ruf** received the B.A. degree in physics from Reed College, Portland, OR, and the Ph.D. degree in electrical and computer engineering from the University of Massachusetts at Amherst. He is currently the Frederick Bartman Collegiate Professor of Climate and Space Science and Director of the Space Institute, University of Michigan, Ann Arbor, MI, and Principal Investigator of the NASA CYGNSS Mission. He has worked previously for Intel Corporation, Aloha, OR, Hughes Space and Communication, El Segundo CA, the NASA Jet Propulsion Laboratory, Pasadena, CA and Penn State University, University Park, PA. His research interests include remote sensing methods, applications, and technology. Prof. Ruf is a member of the National Academy of Engineering, fellow of the American Meteorological Society and IEEE, Vice Chair for Commission F of the U.S. National Committee of the International Radio Science Union, and a member of the American Geophysical Union. He is former Editor-in-Chief of the IEEE Transactions on Geoscience and Remote Sensing and has served on the Editorial Board of Radio Science, the Journal of Atmospheric and Oceanic Technology, and Scientific Reports.



**Joel T. Johnson** received the bachelor's degree in electrical engineering degree from the Georgia Institute of Technology, Atlanta, GA, USA, in 1991, and the S.M. and Ph.D. degrees from the Massachusetts Institute of Technology, Cambridge, MA, USA, in 1993 and 1996, respectively.

He is currently a Professor with the ElectroScience Laboratory, Department of Electrical and Computer Engineering, The Ohio State University, Columbus, OH, USA. His current research interests include the areas of microwave remote sensing, propagation, and electromagnetic wave theory.

Dr. Johnson is a member of commissions B and F of the International Union of Radio Science (URSI), Tau Beta Pi, Eta Kappa Nu, and Phi Kappa Phi. He received the 1993 Best Paper Award from the IEEE Geoscience and Remote Sensing Society, was named an Office of Naval Research Young Investigator, the National Science Foundation Career Awardee, the PECASE Award Recipient in 1997, and was recognized by the U.S. National Committee of URSI as a Booker Fellow in 2002. He served as Technical Program Co-Chair for the 2017 International Geoscience and Remote Sensing Symposium. He has served as an Associate Editor for the Transactions on Geoscience and Remote Sensing since 2000. He is also a Past Chair of the GRSS Technical Committee on Frequency Allocations in Remote Sensing.



**Darren S. McKague** received the Ph.D. degree in Astrophysical, Planetary, and Atmospheric Sciences from the University of Colorado, Boulder, in 2001. He is an Associate Research Scientist in the Department of Climate and Space Sciences and Engineering at the University of Michigan. Prior to working for Michigan, he worked as a systems engineer for Ball Aerospace and for Raytheon, and as a research scientist at Colorado State University. His work has focused on remote sensing with emphases on the development of space-borne microwave remote sensing hardware, microwave remote sensor calibration techniques, and on mathematical inversion techniques for geophysical retrievals. His experience with remote sensing hardware includes systems engineering for several advanced passive and active instrument concepts and the design of the calibration subsystem on the Global Precipitation Mission (GPM) Microwave Imager (GMI) as well as the development of calibration and inter-calibration techniques for the GPM constellation. His algorithm experience includes the development of a near-real time algorithm for the joint retrieval of water vapor profiles, temperature profiles, cloud liquid water path, and surface emissivity for the Advanced Microwave Sounding Unit (AMSU) at Colorado State University, and the development of the precipitation rate, precipitation type, sea ice, and sea surface wind direction algorithms for the risk reduction phase of the Conical scanning Microwave Imager/Sounder (CMIS).



**Anthony Russel** received the B.S. degree in computer science engineering from Michigan State University, East Lansing, MI, USA, in 2014. He is a member of the engineering staff with the Space Physics Research Laboratory, College of Engineering, University of Michigan, Ann Arbor, MI, USA. His primary engineering activities involve algorithm development and large-scale data processing as a member of the Science Operations Center for the CYGNSS mission.



**William L. Wells** is a Staff Systems Engineer in the Department of Space Instrumentation at Southwest Research Institute. He has over 17 years of experience spanning all phases of space mission development and execution. His career focus is systems engineering for constellation missions. He is concurrently the Operations Phase Systems Engineering lead for the Cyclone Global Navigation Satellite System (CYGNSS) mission and the Project Systems Engineer for the Polarimeter to Unify the Corona and Heliosphere (PUNCH) mission. He holds a Bachelor's degree in Aerospace Engineering from The University of Texas at Austin.



**Tianlin Wang** Tianlin Wang (Senior Member, IEEE) received the B.E. degree in electrical engineering from East China University of Science and Technology, Shanghai, China, in 2009; the M.S. degree in radio physics from Fudan University, Shanghai, China, in 2012; and the Ph.D. degree in electrical engineering from the University of Michigan, Ann Arbor, MI, USA, in 2021. He is currently a Research Technologist with the Earth Science Section at the Jet Propulsion Laboratory, California Institute of Technology, Pasadena, CA, USA. Prior to this, he was a President's Postdoctoral Scholar with the Department of Electrical and Computer Engineering and the ElectroScience Laboratory, The Ohio State University, Columbus, OH, USA, from 2021 to 2023. His research interests include microwave remote sensing, microwave measurements, radio-frequency (RF) circuits, and wave propagation and scattering. Dr. Wang is a member of Tau Beta Pi, Eta Kappa Nu, and the American Geophysical Union (AGU). He received the 2018 IEEE Mikio Takagi Student Prize, an Outstanding Student Presentation Award at the 2018 AGU Fall Meeting, the 2021 Ernest K. Smith USNC-URSI Student Prize (second place), and Young Scientist Awards from the 44th Photonics and Electromagnetics Research Symposium and the XXXVth URSI General Assembly and Scientific Symposium in 2023. He currently serves as Chair of the Modeling in Remote Sensing (MIRS) Technical Committee and the Chapters Committee of the IEEE Geoscience and Remote Sensing Society (GRSS).



**Dorina Twigg** received a B.S.E. degree in computer engineering from the University of Michigan, Ann Arbor, MI, USA, an M.S. degree in computer science from Wayne State, Detroit, MI USA, in 2012. She is a member of the engineering staff with the Space Physics Research Laboratory, College of Engineering, University of Michigan, Ann Arbor, MI, USA, and has a lead role in satellite commanding and scientific data processing with the Science Operations Center for the CYGNSS NASA Earth Venture mission.